Scaling laws for drop impingement on porous films and papers

Young Soo Joung and Cullen R. Buie*

Department of Mechanical Engineering, Massachusetts Institute of Technology, 77 Massachusetts Avenue, Cambridge, Massachusetts 02139, USA

(Received 11 June 2013; published 21 January 2014)

This study investigates drop impingement on highly wetting porous films and papers. Experiments reveal previously unexplored impingement modes on porous surfaces designated as necking, spreading, and jetting. Dimensional analysis yields a nondimensional parameter, denoted the Washburn-Reynolds number, relating droplet kinetic energy and surface energy. The impingement modes correlate with Washburn-Reynolds number variations spanning four orders of magnitude and a corresponding energy conservation analysis for droplet spreading shows good agreement with the experimental results. The simple scaling laws presented will inform the investigation of dynamic interactions between porous surfaces and liquid drops.

DOI: 10.1103/PhysRevE.89.013015 PACS number(s): 47.56.+r, 47.55.nb, 47.55.D−

I. INTRODUCTION

Interesting phenomena can be observed when a liquid droplet impacts a liquid or solid surface. Crown formation of milk droplets upon impact with water represents a well-known example of this phenomena [1]. Recently, however, drop impingement on solid surfaces has gained significant attention. This is largely due to state of the art micro- and nanofabrication methods which have enabled novel functional surfaces. Among the functionalized surfaces, superhydrophobic surfaces have been a major thrust [2,3] in part due to their unique impingement properties. Conversely, drop impingement on highly wetting porous films or paper has been largely neglected. Though there have been investigations of the dynamics of droplets on porous media [4–8], most studies have explored thick surfaces where the droplet radius is negligible compared to the substrate thickness.

In this study we investigate droplet dynamics on highly wetting thin porous surfaces. First, we present a modified energy equation accounting for capillary effects that successfully captures droplet spreading upon impact on highly wetting porous surfaces. The modified energy equation reveals a dimensionless parameter denoted the capillary-Weber number, which expresses the relative influence of the matrix potential and the kinetic energy of the impinging drop. Additionally, dimensional analysis leads to a nondimensional parameter, which we will call the Washburn-Reynolds number (Re_W), which strongly correlates with impingement modes on highly wetting porous surfaces. The Washburn-Reynolds number balances inertial effects of the impinging droplet and capillary transport in the porous film.

II. EXPERIMENTAL METHODS

Electrophoretic deposition (EPD) and breakdown anodization (BDA) were used to produce highly wetting micro- and nanoporous surfaces [9,10]. For EPD, TiO_2 nanoparticles (20 nm, anatase, Sigma-Aldrich) and acetic acid were used to make 1 g/liter TiO_2 suspensions. Electric potentials up to 120 V were supplied for 10–30 min during the anodization process to make thin films on the substrate. De-ionized (DI) water pH was adjusted to $p\mathrm{H} = 3$ using nitric acid (70% ACS reagent, Sigma-Aldrich) for the electrolyte during BDA. The electrolyte was maintained at a specified temperature using a water reservoir surrounding the BDA cell. Titanium plates (Ultra Corrosion-Resistant Titanium Grade 2, 0.020 in. thick, McMaster) were used as anode and cathode for both EPD and BDA. BDA was conducted first to make microporous layers followed by EPD of TiO_2 nanoparticles on the microporous layers to realize hierarchical structures. In BDA, the electric potential and the anodization time were varied to obtain different surface properties. In EPD, however, the same conditions were used on each surface to provide consistent nanoscale features. BDA results in microscale porous titania surfaces on titanium substrates [Fig. 1(a)]. Nanoscale porous layers were produced by EPD on the microporous surfaces with titanium dioxide nanoparticles [Fig. 1(b)].

The resulting surfaces display effective contact angles near 0° with high capillary pressures and spreading speeds. The porous surfaces showed near perfect wetting for several liquids including water, ethanol, ethylene glycol, and glycerol. The surfaces can be characterized with respect to capillary pressure, P_{cap}, and spreading speed constant, C_{cap}, through capillary rise measurements [12]. The capillary rise height, h, can be expressed as $h^2 = \frac{1}{2}C_{\mathrm{cap}}t$ (Washburn's equation) [13], with $C_{\mathrm{cap}} = \gamma r_c \cos\theta/\mu$, and r_c is the effective capillary radius, γ is the liquid surface tension, θ is the native contact angle of capillary surface, and μ is dynamic viscosity of the liquid. The value of C_{cap} can be determined by the gradient of the time-dependent experimental capillary rise height. Capillary pressure can be obtained from the maximum rise height, h_{max}, and is expressed by $P_{\mathrm{cap}} = \rho g h_{\mathrm{max}} = 2\gamma\cos\theta/r_c$.

When liquid droplets impact the surfaces, we observed four impingement modes (Fig. 2). We find that impingement modes are determined by the value of $\mathrm{Re}_W = U_o \rho r_c \cos\theta/\mu$. Mode A1 consists of oscillating and spreading of the droplet. In Mode A2 the droplets show necking followed by fast spreading. Mode B consists of smooth spreading without oscillations or necking. Finally, Mode C is characterized by radial jetting and spreading. The Supplemental Material contains a high-speed video with examples of each impingement mode [14].

*crb@mit.edu

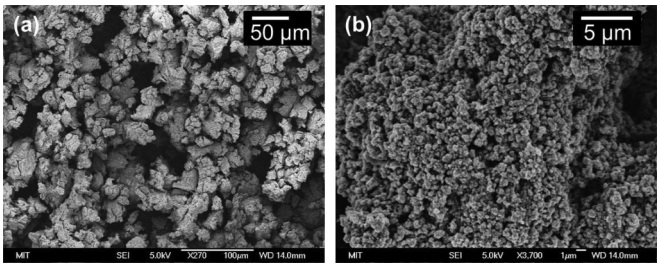

FIG. 1. Scanning electron microscope (SEM) images of as-prepared surfaces show microscale and nanoscale porous structures produced by breakdown anodization (BDA) (a) and electrophoretic deposition (EPD) (b), respectively [11]. The combined BDA/EPD process yields highly wetting micro- and nanoscale hierarchical porous structures.

III. THEORY

Energy conservation is employed to predict droplet spreading upon impact. The energy conservation approach has shown good agreement with experiments, and it has helped to find useful scaling parameters for droplet dynamics [16–18]. In this study we modify the energy equation with two additional terms accounting for viscous dissipation inside porous media and the matrix potential, which we denote as Φ_c and E_{mp}, respectively. The modified energy equation can be expressed as

$$\dot{E}_k + \dot{E}_g + \dot{E}_s + \dot{E}_{mp} + \Phi_l + \Phi_v + \Phi_c = 0, \qquad (1)$$

where E_k is the droplet kinetic energy, E_g is the gravitational potential energy, E_s is the surface energy of the droplet, Φ_l is line dissipation, and Φ_v is viscous dissipation inside the droplet.

For simplicity, we model water droplets impacting solid surfaces as cylinders with a time-dependent radius, $R(t)$, and height, $H(t)$ (Fig. 3) [16,17]. The model droplet has the same volume as the actual droplet. Assuming mass conservation (neglecting evaporation) and fluid incompressibility, the height and radius have the following relationship:

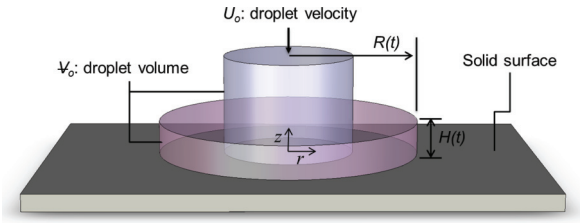

FIG. 3. (Color online) Schematic diagram of the cylindrical droplet impact model with time-dependent radius, $R(t)$, and height, $H(t)$. The model cylindrical droplet has the same volume and impact velocity as the actual droplet.

$$H(t) = \frac{V_o}{\pi R(t)^2},$$

where V_o is the volume of the actual droplet with an initial diameter, D_o. The modeled droplet has the same impact velocity as the actual droplet and thus the same kinetic energy.

A. Kinetic energy

The kinetic energy of a droplet after impact can be calculated from the internal velocity field in the droplet. In the cylindrical model, we assume flow in the droplet is irrotational [19]. The vertical flow velocity, v_z, and the radial flow velocity, v_r, can be defined as

$$v_z = -2\frac{z}{R}\frac{dR}{dt} \quad \text{and} \quad v_r = \frac{r}{R}\frac{dR}{dt}.$$

These velocities are internal flow velocities at a specific instant such that R and dR/dt are spatially independent. The kinetic

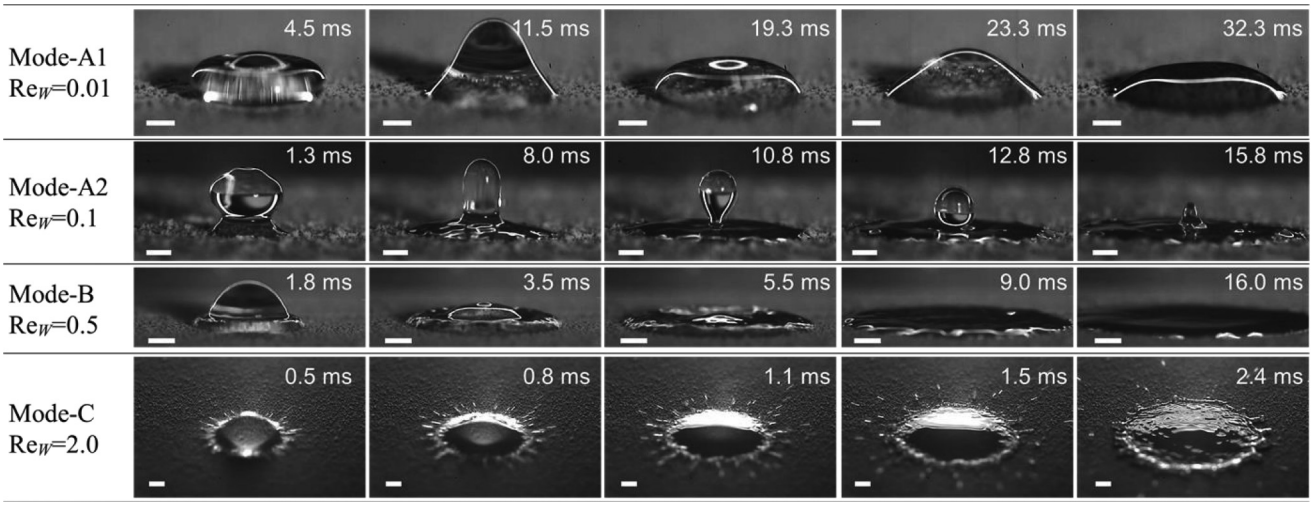

FIG. 2. Droplets show four different impingement modes depending on the Washburn-Reynolds number after impacting highly wetting porous surfaces. The Washburn-Reynolds number can be expressed as $\mathrm{Re}_W = U_o \rho r_c \cos\theta/\mu$, where U_o is the impact velocity, ρ is the liquid density, r_c is the effective capillary radius, θ is the surface contact angle, and μ is the liquid viscosity. Mode A1: compressing-oscillating, Mode A2: necking and spreading, Mode B: spreading, and Mode C: radial jetting and spreading (see Supplemental Material [14]). A high-speed camera (Photron) was used to record the behavior of liquid droplets on the surfaces. The scale bar in each image is 1 mm.

energy of the droplet can be obtained by integrating the internal velocities over the droplet volume, $\forall_o$, as follows:

$$E_k = \frac{1}{2}\rho \int_{\forall_o} \left(v_z^2 + v_r^2\right) d\forall$$
$$= \frac{\rho \forall_o}{2}\left(\frac{1}{2} + \frac{4}{3}\frac{\forall_o^2}{\pi^2 R^6}\right)\left(\frac{dR}{dt}\right)^2$$
$$= E_{k,o}\left(\frac{1}{8} + \frac{16}{27}\frac{1}{R^{*6}}\right)\left(\frac{dR^*}{dt^*}\right)^2, \quad (2)$$

with the initial droplet kinetic energy, $E_{k,o} = \frac{1}{2}\rho \forall_o U_o^2$, the dimensionless drop radius, $R^* = R(t)/(D_o/2)$, and the dimensionless time, $t^* = t(U_o/D_o)$.

B. Gravitational energy

Utilizing the location of the time-dependent center of mass, $H(t)/2$, gravitational energy can be determined:

$$E_g = \rho g \forall_o \frac{H(t)}{2} = \frac{\rho g \forall_o^2}{2\pi R^2} = E_{g,o}\frac{2}{3}\frac{1}{R^{*2}}, \quad (3)$$

where the initial droplet gravitational energy is defined as $E_{g,o} = \frac{1}{2}\rho g \forall_o D_o$.

C. Droplet surface energy

The surface energy of a droplet on a solid surface can be calculated by integrating the surface tension of the entire surface, A. In the cylindrical impact model, the surface tension of the liquid-solid interface can be obtained with Young's equation, and the surface energy is found to be

$$E_s = \int_A \gamma dA = \gamma\left(A_{\text{air}} - A_{\text{wet}}\cos\theta_e\right),$$

where A_{air} is the droplet surface area in contact with air, A_{wet} is the wetted area (the projected area of the solid-liquid interface), and θ_e is the equilibrium contact angle on the surface. Since the surfaces used in this work exhibit complete wetting (i.e., contact angle near zero), the equation for a cylindrical droplet can be reduced as follows:

$$E_s = 2\pi\gamma RH = \frac{2\gamma \forall_o}{R} = \frac{2}{3}\frac{\pi\gamma D_o^2}{R^*} = \frac{2}{3}\frac{E_{s,o}}{R^*}, \quad (4)$$

with the initial droplet surface energy, $E_{s,o} = \pi\gamma D_o^2$.

D. Line dissipation

Dissipation occurs in the process of moving the contact line and the amount is proportional to the contact line speed, v_R, and an effective viscosity, μ_L. According to the de Gennes approach [20], the line dissipation can be expressed by

$$\Phi_l = \frac{1}{2}\mu_L \int_S v_R^2 dS = \mu_L \pi R\left(\frac{dR}{dt}\right)^2$$
$$= \frac{1}{8}\mu_L \pi D_o U_o^2 R^*\left(\frac{dR^*}{dt^*}\right)^2 = \Phi_{l,o}\frac{R^*}{4}\left(\frac{dR^*}{dt^*}\right)^2 \quad (5)$$

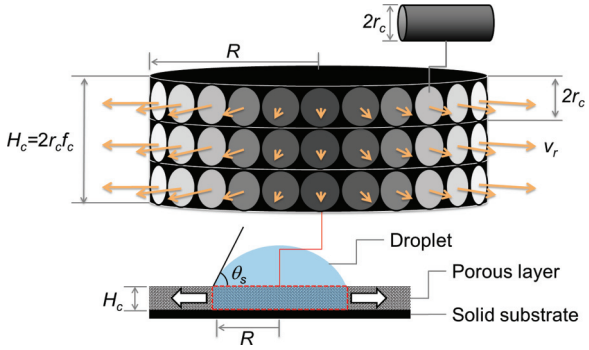

FIG. 4. (Color online) Schematic diagram of capillary flow for the assumed cylindrical droplet geometry. The porous region can be considered as several cylindrical capillaries in parallel, each having a height, $2r_c$. The porous region has height, H_c, and the flow velocity, v_r, at a distance, $R(t)$, from the center, assuming the ratio of the height of the porous region to the initial droplet diameter, H_c/D_o, is small. θ_s is the sliding contact angle, the contact angle of the droplet on the top surface of the porous layer during spreading.

where S is the moving contact line, v_R is the line velocity, $\Phi_{l,o} = \frac{1}{2}\mu_L \pi D_o U_o^2$, and μ_L can be obtained from

$$\mu_L = \mu\frac{3l^*}{\theta_s},$$

where $l^* = \ln(l_{\max}/l_{\min})$ with maximum length scale, $l_{\max}$ (the droplet diameter), minimum length scale, $l_{\min}$ (the microscopic length scale, $2r_c$ in this work), and θ_s, the sliding contact angle, which is the contact angle at the interface of the droplet, the top surface of the porous layer, and air when the droplet is spreading, as shown in Fig. 4. In other words, the sliding contact angle is the advancing contact angle of the spreading droplet. Sliding contact angles were experimentally obtained from high-speed images at $2R/D_o = 2.5$ when the actual droplets were spreading after impact. For example, to obtain Fig. 6, sliding contact angles were determined to be 2.6°, 2.9°, 7.4°, 5.7°, and 19.6° for water, ethanol, ethylene glycol, a 60/40 (v/v) glycerol and water mixture, and a 90/10 (v/v) glycerol and water mixture, respectively.

E. Viscous dissipation inside a droplet

The total viscous dissipation in the boundary layer can be found by integrating the shear stress, τ, multiplied by slip velocity, v_s, for the no-slip area, A_s. To calculate the shear stress generated in the boundary layer inside the droplet, the boundary layer thickness must be estimated. It is clear that the boundary layer thickness is time dependent from lubrication theory, and the time-dependent boundary layer thickness has shown close agreement with experimental results [21,22]. However, to simplify the analysis, we employ a time-independent boundary layer thickness assuming irrotational flow inside the droplet. In the literature [17–19,23], others have successfully formulated the kinetic energy and the viscous dissipation assuming irrotational flow and time-independent boundary layer thickness to predict the droplet behaviors. To calculate the shear stress, we assumed that the effective boundary layer thickness is $D_o/(2f_b)$, where f_b is a correction factor, which was proposed by Bechtel *et al.* [18]. The

slip velocity, v_s, was assumed to be the radial velocity, v_r, and the no-slip area is equal to the projected area of the cylinder. Thus, we obtain the following expression for viscous dissipation:

$$\Phi_v = \int_{A_s} \tau v_s dA \approx \int_{A_s} f_b \mu \frac{v_r}{D_o} v_r dA = \frac{\pi}{2} \frac{f_b \mu}{D_o} R^2 \left(\frac{dR}{dt}\right)^2 = \Phi_{v,o} \frac{3}{64} f_b R^{*2} \left(\frac{dR^*}{dt^*}\right)^2, \quad (6)$$

with

$$\Phi_{v,o} = \mu \mathcal{V}_o \left(\frac{2U_o}{D_o}\right)^2 \quad \text{and} \quad f_b = \sqrt{\frac{\pi}{\mathrm{Oh}}},$$

where the Ohnesorge number is $\mathrm{Oh} = \mu/(\rho\gamma D_o)^{1/2}$.

F. Matrix potential

Matrix potential is the surface energy inside the capillary network that drives fluid transport [24]. The matrix potential is proportional to the wetted volume of the porous region and the capillary pressure [25]. Taking the droplet as the system of interest, work is done on the droplet so the matrix potential can be expressed as

$$E_{mp} = -\int_{\mathcal{V}_{\mathrm{wet}}} P_{\mathrm{cap}} d\mathcal{V} = -\pi P_{\mathrm{cap}} H_c R^2 = -E_{mp,o} f_c R^{*2}, \quad (7)$$

where $\mathcal{V}_{\mathrm{wet}}$ is the wetted volume of the porous region, H_c is the height of the porous region shown in Fig. 4, f_c is the ratio of the height of the porous region to the pore diameter, $2r_c$ ($f_c = H_c/2r_c$) (Fig. 4), and $E_{mp,o}$ is the reference matrix potential,

$$E_{mp,o} = 2r_c P_{\mathrm{cap}} \pi \left(\frac{D_o}{2}\right)^2.$$

Here, the thickness, H_c, is the average height of the porous layer considering its void volume measured by a profilometer (measurement system: Tencor P-16 Surface Profilometer). The negative sign indicates that energy is put into the droplet.

G. Viscous dissipation inside porous media

The shear stress, τ_c, in the porous region can be approximated in the same manner used to estimate the viscous dissipation in the droplet [Eq. (6)] as follows:

$$\tau_c \approx f_c \mu \frac{v_r}{r_c},$$

where v_r is the flow velocity in the porous region at a distance R from the center of the droplet (Fig. 4). If we assume that the contact line of the droplet coincides with the wetted boundary of the porous region, the total viscous dissipation inside the porous region can be expressed as

$$\Phi_c = \int_{A_s} \tau_c v_r dA \approx \frac{\pi}{2} \frac{f_c \mu}{r_c} R^2 \left(\frac{dR}{dt}\right)^2 = \Phi_{c,o} \frac{1}{16} R^{*2} \left(\frac{dR^*}{dt^*}\right)^2, \quad (8)$$

where A_s is the no-slip area of the porous region and the characteristic viscous dissipation can be expressed as

$$\Phi_{c,o} = \mu \mathcal{V}_{\mathrm{wet},o} \left(\frac{U_o}{r_c}\right)^2,$$

and the reference volume of the wetted porous region is $\mathcal{V}_{\mathrm{wet},o} = \pi H_c D_o^2/4$.

H. Energy conservation equation

When Eqs. (2)–(8) are substituted into Eq. (1), the final energy conservation equation can be obtained as a function of the time-dependent droplet radius,

$$\frac{U_o}{D_o}\frac{d}{dt^*}\left(E_{k,o}\left(\frac{1}{8}+\frac{16}{27}\frac{1}{R^{*6}}\right)\left(\frac{dR^*}{dt^*}\right)^2 + E_{g,o}\frac{2}{3}\frac{1}{R^{*2}} + \frac{2}{3}\frac{E_{s,o}}{R^*} - E_{mp,o} f_c R^{*2}\right) + \Phi_{l,o}\frac{R^*}{4}\left(\frac{dR^*}{dt^*}\right)^2 + \Phi_{v,o}\frac{3}{64} f_b R^{*2}\left(\frac{dR^*}{dt^*}\right)^2 + \Phi_{c,o}\frac{1}{16}R^{*2}\left(\frac{dR^*}{dt^*}\right)^2 = 0.$$

We can divide this equation by $E_{k,o}(U_o/D_o)$ to obtain a dimensionless energy equation:

$$\frac{d}{dt^*}\left[\left(\frac{1}{8}+\frac{16}{27}\frac{1}{R^{*6}}\right)\left(\frac{dR^*}{dt^*}\right)^2 + \frac{2}{3}\frac{1}{\mathrm{Fr}}\frac{1}{R^{*2}} + \frac{8}{\mathrm{We}}\frac{1}{R^*} - \frac{12}{\mathrm{We_c}}R^{*2}\right] + \frac{3}{2}\frac{1}{\mathrm{Re}} f_L R^* \left(\frac{dR^*}{dt^*}\right)^2 + \frac{3}{8}\frac{1}{\mathrm{Re}} f_b R^{*2}\left(\frac{dR^*}{dt^*}\right)^2 + \frac{3}{8}\frac{1}{\mathrm{Re_c}} f_c R^{*2}\left(\frac{dR^*}{dt^*}\right)^2 = 0. \quad (9)$$

Here, the initial drop diameter, D_o, and impact velocity, U_o, are used to formulate a dimensionless time, $t^* = t/(D_o/U_o)$, and $f_L = \mu_L/\mu$ is the dimensionless contact line viscosity. The first term is the kinetic energy of the droplet. The gravitational energy and the surface energy are a function of the Froude number, $\mathrm{Fr} = U_o^2/gD_o$, and the Weber number, $\mathrm{We} = \rho D_o U_o^2/\gamma$, respectively. The matrix potential is a function of the capillary-Weber number, $\mathrm{We_c}$, where

$$\mathrm{We_c} = \frac{\rho D_o U_o^2}{f_c \gamma \cos\theta} \sim \frac{E_{k,o}}{E_{mp,o}} = \frac{\frac{1}{2}\rho \mathcal{V}_o U_o^2}{\mathcal{V}_{\mathrm{wet},o} P_{\mathrm{cap}}}. \quad (10)$$

The capillary-Weber number is the ratio of the initial kinetic energy ($E_{k,o}$) of the droplet to the reference matrix potential ($E_{mp,o}$) corresponding to the initial wetted volume [$\mathcal{V}_{\mathrm{wet},o} = \pi(D_o/2)^2 H_c$] of the surface. In the case of either $H_c = 0$ (no porous region) or $\theta = 90°$ (nonwetting), the capillary energy term is negligible. In the dissipation terms, we can see the dimensionless contact line viscosity, $f_L = \mu_L/\mu$, the Reynolds number, $\mathrm{Re} = \rho D_o U_o/\mu$, and the capillary-Reynolds number, $\mathrm{Re_c} = \rho r_c U_o/\mu$.

To solve Eq. (9) numerically, the initial conditions were specified in order to yield the same surface energy and kinetic energy as the real droplet [17]. Therefore, the radius and the impact velocity of the cylindrical model droplet

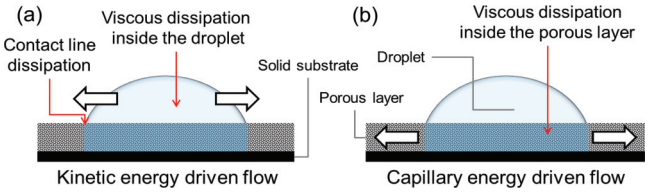

FIG. 5. (Color online) Schematic illustrations of droplet spreading on highly wetting porous surfaces. (a) At high capillary-Weber numbers ($We_c > 10^3$), the kinetic energy determines droplet expansion, while the contact line and viscous effects dissipate mechanical energy. (b) At low capillary-Weber numbers ($We_c < 10$), the capillary energy (matrix potential energy) governs droplet spreading, and viscous dissipation is most prominent inside the porous region.

are slightly different from those of the real droplet used in the drop impingement experiment. First, we set the initial radius of the cylindrical model droplet as $R(0) = D_o/2$. The initial height of the cylindrical model droplet, $H(0)$, can be calculated using mass conservation as $H(0) = \forall_o/[\pi R(0)^2]$, where $\forall_o = (1/6)\pi D_o^3$. The cylindrical model droplet has the same initial surface area as the real droplet, $A_{\text{model}} = A_{\text{real}}$, where A_{model} and A_{real} are the surface areas of the cylindrical model droplet with radius $R(0)$ and the real droplet with radius R_{real}, respectively. This information is used to calculate the initial radius of the cylindrical model droplet. The cylindrical model droplet has the same initial kinetic energy as the real droplet; $\frac{1}{2}\rho \forall_o U_o^2 = \frac{1}{2}\rho \forall_{\text{real}} U_{\text{real}}^2$, where $\forall_{\text{real}}$ and U_{real} are the volume and the impact velocity, respectively, of the real droplet used in the experiment. The initial droplet spreading speed, $dR/dt|_{t=0}$, can be calculated using Eq. (2). As a result, the initial conditions for Eq. (9) are $R^*(0) = 1$ and $dR^*/dt^*|_{t=0} = 1.18$.

We find that each dissipation term in Eq. (9) has different significance depending on We_c, as shown schematically in Fig. 5. Contact line dissipation and viscous dissipation inside the droplet are important at high We_c [Fig. 5(a)]. However, for low We_c ($We_c < 10$), viscous dissipation inside the porous region is the main dissipation term in Eq. (1). As depicted in Fig. 5(b), line dissipation and viscous dissipation are negligible at low We_c because droplet expansion can be considered as a free surface flow driven by the capillary pressure in the porous region.

IV. RESULTS AND DISCUSSION

In Fig. 6 we compare the predicted droplet spreading obtained from Eq. (9) with the experimental results when $We_c > 10^3$. The liquid and surface properties utilized are given in Table I. As suggested in Fig. 5, viscous dissipation inside the porous layer was not considered in the energy equation for high We_c. The surfaces showed varying P_{cap} and C_{cap} values depending on the liquid utilized. The predicted droplet spreading is in good agreement with the experimental data (Fig. 6). This suggests that the matrix potential is essential to appropriately predict droplet spreading. In spite of the geometrical simplifications, the energy equation captures the major energy transfer mechanisms during impingement.

We derived simplified energy conservation equations for four cases with different We, Fr, and We_c regimes to investigate

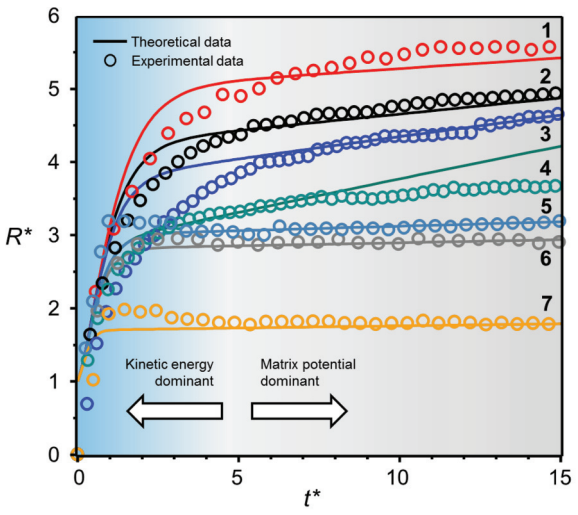

Data	Surface	Fr	We	We_c	$Re_{f_L}^{-1}$	$Re_{f_b}^{-1}$	$Re_c f_c^{-1}$	Re_W	Mode
1	A	355	374	14700	27.9	258.0	83.4	2.1	B
2	A	212	224	7100	21.6	199.5	64.5	1.6	B
3	A	69	73	4100	12.3	114.1	36.8	0.9	B
4	G	89	149	1400	7.0	91.8	16.6	1.9	B
5	I	265	402	15200	8.0	82.9	47.4	1.9	B
6	H	427	772	17800	6.8	76.7	38.8	1.7	B
7	J	205	327	17800	1.5	146.0	1.7	0.1	A1

FIG. 6. (Color online) Theoretical and experimental droplet spreading for multiple liquids after impact on highly wetting porous surfaces. Solid lines represent spreading radii obtained from Eq. (9) while circles are experimental data. The impact velocities are selected such that We_c exceeds 10^3. The table provides the surface and liquid properties and the dimensionless parameters of the energy equation for each data set. Viscous dissipation inside the porous layer, which is the column highlighted in gray in the table, is not considered when $We_c > 10^3$. Here we only considered impingement Modes A1 and B because the droplet mass is not conserved in Modes A2 and C due to necking and jetting behavior, respectively.

the dependence of $R^*(t)$ on each dimensionless parameter. To simplify the expressions, we ignored the constant values of each term and consider the line dissipation dominant because $\text{Re} f_L^{-1}$ is smaller than the other dissipation terms, as shown in Fig. 6. In addition, the initial conditions of $R^*(0) = 0$ and/or $dR^*/dt^*|_{t=0} = 1$ are used to derive the simplified energy conservation expressions as functions of dimensionless parameters. These initial conditions are different from those of the numerical solutions shown in Fig. 6. Table II provides a summary of the simplified energy equations and the dimensionless droplet radius change with different ranges of We, Fr, and We_c. From Table II, we see that the gravitational energy and the surface energy do not significantly affect droplet spreading. The kinetic energy influences expansion largely in the initial stage of impact, and the radius is asymptotic to a specific value dependent upon the Re. With respect to the matrix potential, the dimensionless droplet radius increases linearly with time, and the expansion rate is proportional to the ratio of Re to We_c. As the matrix potential is dominant in Table II, Eq. (9) can be simplified to $dR^*/dt^* \sim \text{Re}/We_c$ for large t^* when the kinetic energy is dissipated ($We_c \ll 1$). This simplified equation means that the droplet expansion rate is determined by the ratio of Re to We_c.

Therefore, theoretically, $R(t)^*$ does not achieve a constant value if the capillary pressure (P_{cap}) is nonzero. In Fig. 6, the curves for highly viscous liquids appear to converge to constant values but in actuality they slightly increase at a rate of $\mathrm{Re}/\mathrm{We_c}$. In Fig. 6, the initial drastic increase of R^* is mainly attributed to the kinetic energy, and the linear increase of R^* after the initial stage of impact is due to the matrix potential. As a result, the assumption that line dissipation is dominant can be justified by comparing the simplified energy equations and the experimental data in Fig. 6. The kinetic energy and the matrix potential are the main driving forces for droplet spreading when $\mathrm{We_c} \gg 1$ and $\mathrm{We_c} \ll 1$, respectively. The initial droplet spreading results from the relationship between line dissipation and kinetic energy. After the kinetic energy is dissipated, the linear droplet spreading is due to the balance between line dissipation and matrix potential. Both spreading regimes are displayed in Fig. 6.

In the case of $\mathrm{We_c} < 10$, viscous dissipation in the porous region is the dominant dissipation mechanism and the other dissipation terms are ignored, as shown in Fig. 5. To justify this assumption, note that $\mathrm{Re_c}$ is small relative to Re in the energy equation. When $\mathrm{Re_c}$ and Re are compared in the dissipation terms, however, we must carefully consider the no-slip area (A_s). In the viscous dissipation inside the droplet and the line dissipation, the contact surface between the droplet and the surface is assumed as the no-slip surface. This assumption is valid when $\mathrm{We_c}$ is sufficiently high ($\mathrm{We_c} > 10^3$). When $\mathrm{We_c}$ is small, however, the no-slip surface becomes a slip boundary because the flows inside the porous layer induce spreading via capillary pressure. Therefore, the viscous dissipation inside the droplet and the line dissipation are negligible when $\mathrm{We_c}$ is small ($\mathrm{We_c} < 10$). Furthermore, gravitational energy and droplet surface energy are much weaker than the matrix potential when $\mathrm{We_c} < 10$ and $R^* > 1$. Therefore, the energy equation becomes a function of the viscous dissipation and matrix potential. In this case Eq. (9) for the dimensionless droplet radius becomes

$$-\frac{d}{dt^*}\left(\frac{12}{\mathrm{We_c}}R^{*2}\right)+\frac{1}{\mathrm{Re_c}}\frac{3}{8}f_c R^{*2}\left(\frac{dR^*}{dt^*}\right)^2=0. \qquad (11)$$

From Eq. (11), the dimensionless droplet expansion rate is found to be

$$\frac{dR^*}{dt^*}=\frac{64}{f_c}\frac{\mathrm{Re_c}}{\mathrm{We_c}}\frac{1}{R^*}=64\frac{C^*_{\mathrm{cap}}}{R^*}. \qquad (12)$$

By integrating Eq. (12), the droplet radius can be expressed as

$$R^{*2}=128\frac{1}{f_c}\frac{\mathrm{Re_c}}{\mathrm{We_c}}t^*=128C^*_{\mathrm{cap}}t^*. \qquad (13)$$

As a result, $R(t)^*$ is only dependent on t^* and C^*_{cap} and the initial condition of Eq. (13) is not needed.

Equation (13) effectively predicts the droplet radius change on wetting surfaces at low $\mathrm{We_c}$, as shown in Fig. 7. Here the independent axis is $C^*_{\mathrm{cap}}t^*$ and the dependent axis is R^{*2} in Fig. 7 to display the linearity of Eq. (13) and the corresponding experimental data. We used $\mathrm{We_c}$ less than 100 for the drop impingement experiments in Fig. 7, but the theoretical data obtained from Eq. (13) assume that $\mathrm{We_c}$ is less than 10. Our intent was to show that the experimental data become closer to the theoretical data when their $\mathrm{We_c}$ is close to 10. As shown in Fig. 7, the experimental data obtained with $\mathrm{We_c}$ higher than 10 show larger deviations from the theoretical data. However, the nearly linear experimental data, obtained when $\mathrm{We_c}$ is higher than 10, are recovered after initial impact because the kinetic energy is dissipated through the initial moments of droplet expansion. $\mathrm{We_c}$ only reflects the initial impact speed of the droplet. Therefore, after the droplet loses its kinetic energy the expansion more closely follows the theoretical prediction. This is why droplets with $\mathrm{We_c}$ higher than 10 show nonlinearity in the initial impact region. It reveals that the droplet expansion rate at low $\mathrm{We_c}$ is governed by the spreading speed constant, C_{cap}. In highly viscous liquids, the initial kinetic energy is dissipated through droplet deformation resulting from viscous effects inside the droplet after impact; therefore the impingement modes of highly viscous liquids are confined to Mode A and mainly governed by the matrix potential.

We can see Modes A1 and B in Fig. 6 (high $\mathrm{We_c}$), and Modes A1 and A2 in Fig. 7 (low $\mathrm{We_c}$). In Figs. 6 and 7, we used the experimental data obtained from Modes A1 and B because the mass conservation is not valid in Modes A2 and C due to necking and jetting behavior, respectively. From the investigation of $\mathrm{We_c}$ and Re_W, we can say that very low and

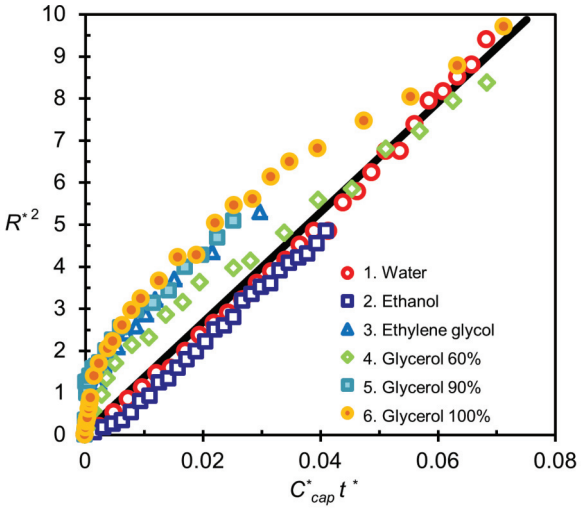

Data	Surface	Fr	We	$\mathrm{We_c}$	$\mathrm{Re}f_L^{-1}$	$\mathrm{Re}f_b^{-1}$	$\mathrm{Re_c}f_c^{-1}$	Re_W	Mode
1	A	0.9	0.9	15	1.38	12.79	4.14	0.1	A2
2	G	0.7	1.2	7	0.63	8.22	1.47	0.2	A2
3	H	0.9	1.6	37	0.75	8.44	1.82	0.2	A1
4	I	1.3	2.0	81	0.57	5.92	3.32	0.1	A1
5	J	15.3	24.4	86	0.35	4.80	0.45	0.003	A1
6	K	0.1	0.2	43	0.01	0.14	0.01	0.002	A1

FIG. 7. (Color online) Experimental results for droplet spreading at low capillary-Weber number for the liquids shown in Table I. The symbols and the black solid line indicate the experimental data when $\mathrm{We_c} < 100$ and the theoretical data obtained from Eq. (13), respectively. Viscous dissipation inside the droplet and line dissipation, which are the columns highlighted in gray in the table, are not considered in the energy equation because $\mathrm{We_c}$ is low. The square of the dimensionless radius change is linearly proportional to the dimensionless time. The table provides the surface properties, liquid properties, and the dimensionless parameters of the energy equation for each data set. The impingement modes are confined to Modes A1 and A2 because $\mathrm{Re}_W < 0.2$ when $\mathrm{We_c} < 100$.

TABLE I. Liquid and surface properties used in the drop impingement experiments and numerical simulations. The properties of the glycerol and water mixture were obtained from the literature [15]. Highly wetting porous titania (TiO_2) surfaces were produced by an electrochemical fabrication method [11]. The porous titania surfaces showed wide variations in capillary pressure and spreading speed. The thin layer chromatography (TLC) plates were obtained from Sigma-Aldrich. The gel-blotting paper is a chromatography paper (grade 230) obtained from Genesee Scientific. The coffee filter is a commercial product made by Melitta USA, Inc. The symbols correspond to the symbols in the plot of drop impingement modes (Fig. 8).

Symbol	Surface	Liquid	Effective pore radius r_c (μm)	Layer thickness H_c (μm)	Droplet diameter D_o (mm)	Surface tension γ (mN/m)	Viscosity μ (cP)	Density ρ (kg/m^3)	Capillary pressure P_{cap} (Pa)	Spreading constant C_{cap} (mm^2/s)
A	Porous titania surface 1	Water	10.6	8.6	2.8	72.8	0.9	998	783	49
B	Porous titania surface 1	Water	10.6	8.6	2.2	72.8	0.9	998	783	49
C	Porous titania surface 1	Water	10.6	8.6	5	72.8	0.9	998	783	49
D	Porous titania surface 2	Water	13.4	9.2	2.8	72.8	0.9	998	1048	104.4
E	Porous titania surface 3	Water	13.1	9.2	2.8	72.8	0.9	998	930	88.6
F	Porous titania surface 4	Water	13	9.2	2.8	72.8	0.9	998	773	72.2
G	Porous titania surface 5	Ethanol	8.85	9.5	2.2	22.3	1.1	789	1084	38.6
H	Porous titania surface 6	Ethylene glycol	28	10.5	2.8	47.3	16	1113	863	21.0
I	Porous titania surface 6	Glycerol 60% +water 40%	25	10.5	3	67	9	1154	733	19.8
J	Porous titania surface 6	Glycerol 90% +water 10%	21	10.5	2.9	63.6	164	1232	665	0.85
K	Porous titania surface 7	Glycerol	13.6	9.4	2.8	63	1258	1261	495	0.37
L	Silica TLC	Water	4.2	250	2.8	72.8	0.9	998	959	9.5
M	Cellulose TLC	Water	5.8	100	2.8	72.8	0.9	998	1076	20.4
N	Aluminum TLC	Water	5.1	250	2.8	72.8	0.9	998	1546	22.4
O	Gel-blotting paper	Water	5.6	340	2.8	72.8	0.9	998	1395	24.0
P	Coffee filter	Water	7.9	120	2.8	72.B	0.9	998	1420	60.4

high We_c numbers correspond to Modes A and C, respectively, because these We_c regimes correspond to low and high Re_W. However, to predict the transition between the impingement modes, viscous dissipation inside the porous region must be considered. From Eq. (13), we see that C_{cap} includes the viscosity effects in the porous region; therefore, Re_W incorporates the effects of kinetic energy, matrix potential, and viscous dissipation. This is why we can predict impingement mode transitions with Re_W. Dimensional analysis is a useful tool to extract pertinent dimensionless groups using parameters obtained from the modified energy equations. Dimensionless groups are formed from the parameters, C_{cap}, P_{cap}, and H_c, which relate to the highly wetting surfaces in addition to the parameters, D_o, U_o, ρ, μ, and γ. We find that a dimensionless parameter obtained from a combination of the dimensionless capillary spreading constant, $C^*_{cap} = C_{cap}/(U_o D_o)$, and the Weber number governs the drop impingement modes. We denote this nondimensional number the "Washburn-Reynolds" due to its similarity to the traditional Reynolds number and its relationship with Washburn's equation [26]. The Washburn-Reynolds number, Re_W, is expressed by

$$Re_W = C^*_{cap} We = \frac{U_o \rho r_c \cos\theta}{\mu}. \tag{14}$$

The spreading speed constant, C_{cap}, is obtained from capillary rise measurements and combined with the Weber

TABLE II. Simplified energy conservation equation and dimensionless droplet radius at different physical regimes. The line dissipation in Eq. (9) is considered dominant and the other dissipation terms are ignored to obtain simplified energy conservation equations as functions of common dimensionless parameters. The dimensionless droplet radius can be expressed as a function of the Reynolds number and another dimensionless parameter; therefore, we can characterize the droplet radius change with respect to the relative influence of the Reynolds number.

Dominant effect	Dimensionless parameters	Simplified energy equation	Dimensionless droplet radius	Characteristic
Kinetic energy	$We \gg 1$, $Fr \gg 1$, $We_c \gg 1$	$\frac{d}{dt^*}\left[\left(\frac{dR^*}{dt^*}\right)^2\right] \approx -\frac{1}{Re} R^* \left(\frac{dR^*}{dt^*}\right)^2$	$R^* = \sqrt{Re}\tanh\left(\sqrt{\frac{1}{Re}} t^*\right)$	Asymptotic to $Re^{1/2}$
Gravitational potential energy	$We \gg 1$, $Fr \ll 1$, $We_c \gg 1$	$\frac{d}{dt^*}\left[\frac{1}{Fr}\left(\frac{1}{R^*}\right)^2\right] \approx -\frac{1}{Re} R^* \left(\frac{dR^*}{dt^*}\right)^2$	$R^* = \left(\frac{Re}{Fr} t^*\right)^{1/5}$	Weak due to $\frac{1}{5}$ power dependence
Surface energy	$We \ll 1$, $Fr \gg 1$, $We_c \gg 1$	$\frac{d}{dt^*}\left(\frac{1}{We}\frac{1}{R^*}\right) \approx -\frac{1}{Re} R^* \left(\frac{dR^*}{dt^*}\right)^2$	$R^* = \left(\frac{Re}{We} t^*\right)^{1/4}$	Weak due to $\frac{1}{4}$ power dependence
Matrix potential energy	$We \gg 1$, $Fr \gg 1$, $We_c \ll 1$	$\frac{d}{dt^*}\left[\frac{1}{We_c}(R^*)^2\right] \approx \frac{1}{Re} R^* \left(\frac{dR^*}{dt^*}\right)^2$	$R^* = \frac{Re}{We_c} t^*$	Linearly proportional to Re/We_c

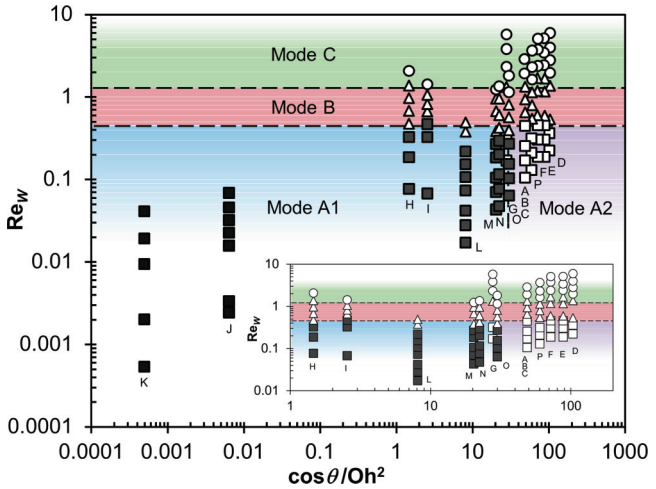

FIG. 8. (Color online) Impingement mode transitions correlate with the Washburn-Reynolds number, as shown in the log-log plot of Re_W vs $\cos\theta/\mathrm{Oh}^2$, where Oh is the Ohnesorge number and θ is the Young's contact angle of the surface. $C_{\mathrm{cap}}/\upsilon$ has the same form of $\cos\theta/\mathrm{Oh}^2$, where υ is the kinematic viscosity of liquids used. Both dimensionless parameters can be used to distinguish wetting properties of the surfaces. Symbols: ■, □, △, and ○ indicate Modes A1, A2, B, and C, respectively. The capital letter under each vertical line indicates the surface name shown in Table I. The inset shows the mode transitions in a narrow $C_{\mathrm{cap}}/\upsilon$ region of 1–100.

number to obtain Re_W. Using the liquids and surfaces in Table I, drop impingement experiments were conducted with varying impact velocities. It is worth noting that when the contact angle is small [$\cos\theta \sim 1$] the Washburn-Reynolds number Re_W is close to the capillary-Reynolds number Re_c, the Reynolds number inside a single capillary tube with radius r_c and flow speed U_o.

When the impingement modes were plotted with respect to We or Re, there were several orders of magnitude differences between mode transitions for different liquids. However, Re_W correlates with mode transitions for a wide range of liquid and surface properties, impact velocities, and for various highly wetting porous surfaces (Fig. 8). As shown in Fig. 8, increasing Re_W governs transitions between impingement modes. Interestingly, in Mode A ($\mathrm{Re}_W < 0.5$), observation of Mode A1 or Mode A2 appeared to vary with $\cos\theta/\mathrm{Oh}^2$, where Oh is the Ohnesorge number expressed as $\mathrm{Oh} = \mu/(r_c\rho\gamma)^{1/2}$ and θ is the Young's contact angle of the surface. This parameter has the same form of another dimensionless group of $C_{\mathrm{cap}}/\upsilon$, where υ is the kinematic viscosity of liquids used. We found that these two dimensionless groups can effectively characterize the wetting ability of surfaces for various liquids. In Mode A1 we believe that kinetic energy is transferred to viscous dissipation through the observed oscillations in the low $\cos\theta/\mathrm{Oh}^2$ region ($\cos\theta/\mathrm{Oh}^2 < 30$). Conversely, for the high $\cos\theta/\mathrm{Oh}^2$ region ($\cos\theta/\mathrm{Oh}^2 > 30$) the matrix potential is compensated by the necking behavior observed in Mode A2. Modes A1 and A2 are combined as Mode A since both are observed in the same Re_W range. Further investigation is needed to illuminate the role of C_{cap} for the transition between Modes A1 and A2. The biggest advantage of the Washburn-Reynolds number is that we can predict the impingement modes based upon three factors: surface properties (r_c and θ), liquid properties (ρ and μ), and impact velocity (U_o). Therefore, once the surface and liquid are determined, we can change the impingement modes using the impact velocity. Alternatively, if the impact velocity is limited to a specific range, the impingement modes can be altered by the surface and liquid properties. However, in this case, the modes available are limited because C_{cap} and μ have narrower ranges than U_o.

The Washburn-Reynolds number (Re_W) can be interpreted as the ratio between the inertia of the impinging droplet and capillary driven transport in the porous thin film. At high Re_W, the droplet inertia is dominant, resulting in Mode C (jetting). In Mode B, the inertial and capillary effects are balanced and smooth spreading is observed. Conversely, Mode A (low Re_W) results in capillary driven flows. When the capillary radius is large and the contact angle is small, the surfaces generally show high spreading speed. This can result in oscillating motions (Mode A1) at low C_{cap} and necking (Mode A2) at high C_{cap}. In Mode A, droplets spread largely due to the matrix potential since the initial droplet kinetic energy is negligible.

V. CONCLUSIONS

In this work, we propose an energy conservation equation to predict droplet spreading on highly wetting porous thin films. Notably, we find that the matrix potential must be included to accurately simulate droplet spreading. This effect can be evaluated with the capillary-Weber number, We_c, which is the ratio of the initial kinetic energy of the impinging droplet to the initial matrix potential. Furthermore, we discovered a dimensionless parameter, the Washburn-Reynolds number (Re_W), which correlates with impingement modes on highly wetting porous surfaces. Re_W can be derived from dimensional analysis or the simplified energy equations at low and high We_c. At high We_c, the Weber number governs the droplet expansion rate but at low We_c numbers, the dimensionless spreading constant, C^*_{cap}, governs droplet spreading. Re_W can be obtained from We and C^*_{cap}. Re_W has the same form as the Reynolds number but possesses an effective length scale, $r_c\cos\theta$, which reflects the wetting properties of the surface. Re_W effectively correlates with impingement modes across a wide range of fluid and surface properties. Re_W provides useful insight into droplet dynamics and can be used to guide the design of highly wetting surfaces for applications ranging from spray cooling to paper microfluidics and inkjet printing.

ACKNOWLEDGMENTS

We are grateful to Mr. Sangok Kim and Professor Sangbae Kim for help with high-speed imaging. The authors are grateful to Dr. Jim Bales and Ms. Sandra J. Lipnoski of the MIT Edgerton Center for sharing their high-speed camera. This work made use of the MRSEC Shared Experimental Facilities at MIT, supported by the National Science Foundation under Award No. DMR-08-19762. Funding was provided by Battelle Memorial Institute.

[1] M. Rein, Fluid Dyn. Res. **12**, 61 (1993).
[2] P. Tsai, S. Pacheco, C. Pirat, L. Lefferts, and D. Lohse, Langmuir **25**, 12293 (2009).
[3] R. Rioboo, M. Voué, A. Vaillant, and J. De Coninck, Langmuir **24**, 14074 (2008).
[4] J. P. Terry and R. A. Shakesby, Earth Surf. Processes Landforms **18**, 519 (1993).
[5] N. Alleborn and H. Raszillier, Chem. Eng. Sci. **59**, 2071 (2004).
[6] A. N. Lembach, H.-B. Tan, I. V. Roisman, T. Gambaryan-Roisman, Y. Zhang, C. Tropea, and A. L. Yarin, Langmuir **26**, 9516 (2010).
[7] N. C. Reis, Jr., R. F. Griffiths, and J. M. Santos, J. Comput. Phys. **198**, 747 (2004).
[8] A. Clarke, T. D. Blake, K. Carruthers, and A. Woodward, Langmuir **18**, 2980 (2002).
[9] Y. S. Joung and C. R. Buie, Langmuir **27**, 4156 (2011).
[10] Y. S. Joung and C. R. Buie, Key Eng. Mater. **507**, 9 (2012).
[11] Y. S. Joung and C. R. Buie, J. Phys. Chem. B **117**, 1714 (2013).
[12] A. Siebold, A. Walliser, M. Nardin, M. Oppliger, and J. Schultz, J. Colloid Interface Sci. **186**, 60 (1997).
[13] E. W. Washburn, Phys. Rev. **17**, 273 (1921).
[14] See Supplemental Material at http://link.aps.org/supplemental/10.1103/PhysRevE.89.013015 for a movie of four different impingement modes of droplets hitting wettable porous surfaces.
[15] Glycerine Producers' Association, *Physical Properties of Glycerine and Its Solutions* (Glycerine Producers' Association, New York, 1963).
[16] H. Y. Kim and J. H. Chun, Phys. Fluids **13**, 643 (2001).
[17] P. Attane, F. Girard, and V. Morin, Phys. Fluids **19**, 012101 (2007).
[18] S. E. Bechtel, D. B. Bogy, and F. E. Talke, IBM J. Res. Dev. **25**, 963 (1981).
[19] X. Yu, Z. Q. Wang, Y. G. Jiang, and X. Zhang, Langmuir **22**, 4483 (2006).
[20] R. Golestanian and E. Raphaël, Phys. Rev. E **64**, 031601 (2001).
[21] I. V. Roisman, Phys. Fluids **21**, 052104 (2009).
[22] S. Tabakova, F. Feuillebois, A. Mongruel, V. Daru, and S. Radev, Z. Angew. Math. Phys. **63**, 313 (2012).
[23] M. Pasandideh-Fard, Y. M. Qiao, S. Chandra, and J. Mostaghimi, Phys. Fluids **8**, 650 (1996).
[24] F. Miller, Microb. Ecol. **18**, 59 (1989).
[25] D. G. Fredlund and H. Rahardjo, *Soil Mechanics for Unsaturated Soils* (John Wiley & Sons, New York, 1993).
[26] The equation typically credited to Washburn is sometimes called the Lucas-Washburn or Bell-Cameron-Lucas-Washburn equation in honor of work by Lucas (1918) and Bell and Cameron (1906) that preceded Washburn's original publication in 1921.